Published in final edited form as:
Microfluid Nanofluidics. 2013 January 1; 14(1-2): 77–87. doi:10.1007/s10404-012-1024-5.

The influence of size, shape and vessel geometry on nanoparticle distribution

Jifu Tan,
Department of Mechanical Engineering and Mechanics, Lehigh University, Bethlehem, PA 18015, USA

Samar Shah,
Department of Mechanical Engineering and Mechanics, Lehigh University, Bethlehem, PA 18015, USA

Antony Thomas,
Bioengineering Program, Lehigh University, Bethlehem, PA 18015, USA

H. Daniel Ou-Yang, and
Bioengineering Program, Lehigh University, Bethlehem, PA 18015, USA. Department of Physics, Lehigh University, Bethlehem, PA 18015, USA

Yaling Liu
Department of Mechanical Engineering and Mechanics, Lehigh University, Bethlehem, PA 18015, USA. Bioengineering Program, Lehigh University, Bethlehem, PA 18015, USA

Yaling Liu: yal310@lehigh.edu

Abstract

Nanoparticles (NPs) are emerging as promising carrier platforms for targeted drug delivery and imaging probes. To evaluate the delivery efficiency, it is important to predict the distribution of NPs within blood vessels. NP size, shape and vessel geometry are believed to influence its biodistribution in circulation. Whereas, the effect of size on nanoparticle distribution has been extensively studied, little is known about the shape and vessel geometry effect. This paper describes a computational model for NP transport and distribution in a mimetic branched blood vessel using combined NP Brownian dynamics and continuum fluid mechanics approaches. The simulation results indicate that NPs with smaller size and rod shape have higher binding capabilities as a result of smaller drag force and larger contact area. The binding dynamics of rod-shaped NPs is found to be dependent on their initial contact points and orientations to the wall. Higher concentration of NPs is observed in the bifurcation area compared to the straight section of the branched vessel. Moreover, it is found that Péclet number plays an important role in determining the fraction of NPs deposited in the branched region and the straight section. Simulation results also indicate that NP binding decreases with increased shear rate. Dynamic NP re-distribution from low to high shear rates is observed due to the non-uniform shear stress distribution over the branched channel. This study would provide valuable information for NP distribution in a complex vascular network.

Keywords

Nanoparticle distribution; Shape effect; Vascular network; Péclet number

Correspondence to: Yaling Liu, yal310@lehigh.edu.

1 Introduction

Nanoparticles (NPs) have been extensively studied in recent years as potential multifunctional carrier platforms for therapeutic drug delivery and imaging applications (Chauvierre et al. 2003; Farokhzad and Langer 2006; Mathiowitz et al. 1997; Nasongkla et al. 2006; Peppas 2006; Roney et al. 2005; Shah 2006; Sukhorukov and Mohwald 2007). To reach the target diseased site, NPs have to marginate toward the vascular wall, interact with the receptors expressed on the vascular wall surface, and finally bind at the target region. The concentration of drug at the targeted site should be high enough to kill the diseased cells with minimal side effects, thus making NP distribution study extremely important in evaluating therapeutic efficacy. NP distribution prediction has been considered to be the top priority in NP drug delivery modeling (Sanhai et al. 2008; Li et al. 2012; Almeida et al. 2011). However, evaluation of NP biodistribution is very complex because it can be influenced by multiple factors including particle size, shape, surface chemistry, and local flow conditions. As a major influence factor, size effect on distribution has been extensively studied. For example, NPs with size between 100 and 200 nm are ideal for tumor delivery due to the enhanced permeability and retention (EPR) effect (Stolnik et al. 1995; Cho et al. 2008; Mitragotri and Lahann 2009). Recent data also reveal that long worm-shaped filomicelles may enhance the circulation time in rodents (Geng et al. 2007; Liu et al. 2012) and are more efficient in killing tumor stroma (Christian et al. 2009). Disk-shaped carriers targeted to intercellular adhesion molecules 1 (ICAM-1) also showed longer half-lives in circulation (Muro et al. 2008). Decuzzi et al. (2010) studied size and shape effect in the biodistribution of intravascularly injected silicon particles with size from 700 to 3 μm, among which discoidal particles accumulate excessively in most organs except liver. The adhesion of nanocarriers depends on targeting antibodies' affinity, surface density, and epitope specificity (Muzykantov et al. 2012). With proper antibodies, long and flexible filomicelles can be targeted to the endothelial surface despite the large drag from the flow (Shuvaev et al. 2011). Inter-particle interaction and particle-copolymer interaction have been identified as two critical repulsive interactions influencing NP aggregates and copolymer/nanoparticles morphology (Chen and Ruckenstein 2009, 2011). Junctions and bifurcations in microvasculature also influence particle adhesion. Preferential particle adhesion near bifurcation was observed in synthetic microvascular networks (Prabhakarpandian et al. 2008; Doshi et al. 2010; Tousi et al. 2010).

Numerical models have been established to study NPs behavior in blood flow. For example, Liu et al. (2010) combined Monte Carlo and weighted histogram analysis method to calculate the nanocarrier binding affinities, and validated them in experiments. Lee et al. (2009) simulated a NP focusing lens in a microfluidic channel. Gentile et al. (2008) studied the transport of NP in blood vessels under the effect of vessel permeability and blood rheology. Longest et al. (2003) simulated the blood particle adhesion process in a non-parallel flow. Decuzzi et al. (2006) studied the adhesive strength of non-spherical particles, formulating a simple mathematical expression for binding probability incorporating several factors such as buoyancy, hemodynamic forces, receptor and ligand density, etc. Shah et al. (2011) modeled the adhesion dynamics of spherical and rod shape NPs and found that rod shape particles have higher binding probability compared to spherical ones under shear flow. Tan et al. (2012) studied the influence of red blood cells (RBCs) on NP transport and dispersion and found RBCs enhance NP binding. However, little is known about the size, shape effect on NP distribution in a vascular network, which consists of straight and branches vessels with various parent and daughter diameters and branching angles (Hoganson et al. 2010). It is believed local shear rate, the geometric structure of the vascular network largely influence NP binding (Prabhakarpandian et al. 2008; Doshi et al. 2010; Tousi et al. 2010). This paper presents a numerical study on NP distribution along a

branched vessel for different NP size, shape, and shear rates. It is expected that such study in a branched vessel will contribute to the understanding of NP delivery in complex vasculature through scaling and analogy. In what follows, we will introduce the computational method first. Then, the simulation results of NP distribution in a branched channel at different shear rates are presented. Discussion and future work are given in the end.

2 Methods

2.1 Brownian dynamics of nanoparticles

Nanoparticles of various sizes and shapes are considered in this paper. The motion of the nanoparticle is governed by the combined effects of drag force from fluid flow, adhesion force from ligand-receptor binding, and Brownian motion. Brownian theory points out that small particles immersed in fluids are subjected to the random collisions from the surrounding liquid molecules (Einstein 1956; Ermak and Mccammon 1978; Li and Ahmadi 1992). Patankar et al. (2004) proposed an algorithm for direct numerical simulation of Brownian motion by adding random disturbance in fluids. At microscale, the Brownian motion is negligible compared to larger drag forces (>50 pN for particle size >1 μm)(Mody and King 2007). At nanoscale, Brownian force outweighs the drag force, becoming a dominant force to drive NP near vessel wall. The random forces **R**(t) and random Torques **T**(t) acting on a NP are responsible for Brownian motion and satisfy the fluctuation–dissipation theorem (Mori et al. 1998):

$$\langle \mathbf{R}_i(t)\rangle=0,\ \langle \mathrm{T}_i(t)\rangle=0, \quad (1)$$

$$\langle \mathbf{R}_i(t)\mathbf{R}_j(t')\rangle=2k_{\mathrm{B}}T\beta_t\delta_{ij}\delta(t-t')\delta \quad (2)$$

$$\langle \mathbf{T}_i(t)\mathbf{T}_j(t')\rangle=2k_{\mathrm{B}}T\beta_{\mathrm{r}}\delta_{ij}\delta(t-t')\delta, \quad (3)$$

where, $\boldsymbol{\delta}$ is the unit-second order tensor, δ_{ij} is the Kronecker delta, $\delta(t-t')$ is the Dirac delta function, $k_{\mathrm{B}}T$ is thermal energy of system, β_{t} and β_{r} are translational and rotation friction coefficient, respectively.

The friction coefficient depends on several physical parameters, such as fluid viscosity, size, and shape of the NP. The friction coefficient for particles can be easily derived from Stokes' law:

$$\beta_{\mathrm{t}}=3\mu d \quad (4)$$

$$\beta_{\mathrm{r}}=\pi\mu d^3 \quad (5)$$

where μ is the fluid viscosity, d is the diameter of particle. The velocity of a particle moving under a deterministic force in a fluid with velocity $\mathbf{V}_{\mathrm{f}}$ is given by:

$$\mathbf{V}_{\mathrm{p}}=\left(\frac{\mathbf{F}_{\mathrm{det}}}{\beta_{\mathrm{t}}}+\mathbf{V}_{\mathrm{f}}\right)+\left(\frac{\mathrm{T}_{\mathrm{det}}}{\beta_{\mathrm{r}}}+\omega_{\mathrm{f}}\right)\times \mathrm{r} \quad (6)$$

where $\mathbf{V}_{\mathrm{f}}$ and ω_{f} are fluid translational and angular velocity vectors, respectively; $\mathbf{V}_{\mathrm{p}}$ is the particle velocity; **r** is the position vector from the centroid of NPs; $\mathbf{F}_{\mathrm{det}}$ and $\mathbf{T}_{\mathrm{det}}$ are the total

deterministic force and torque acting on the NP (including Brownian force/torque, adhesion force/torque, etc.).

The fluid in the simulation is assumed to be an incompressible viscous fluid governed by the Navier–Stokes equations:

$$\rho\left(\frac{\partial \mathbf{v}_f}{\partial t}+\mathbf{v}_f\cdot\nabla\mathbf{v}_f\right)=-\nabla p+\mu\nabla^2\mathbf{v}_f \quad (7)$$

$$\nabla\cdot\mathbf{v}_f=0 \quad (8)$$

where $\mathbf{v}_f$ is the fluid velocity in the fluid domain. The equations are solved through finite element method. The Petrov–Galerkin weak forms of the system and other details can be found in previous publications (Liu et al. 2007). The nonlinear system is solved using the Newton–Raphson method. Moreover, generalized minimum residual (GMRES) iterative algorithm is employed to improve computation efficiency and to compute residuals based on matrix-free techniques (Saad and Schultz 1986).

2.2 Receptor-ligand binding model

When NPs are in contact with receptor-expressed wall, ligands coated on the NP surface bind with receptors on the wall. The receptor-ligand binding process can be described by an equation developed by Bell and Ward (Bell 1978; Bell et al. 1984; Ward and Hammer 1993):

$$\frac{\partial N_b}{\partial t}=k_f(N_l-N_b)(N_r-N_b)-k_rN_b \quad (9)$$

where N_b is the number of formed receptor-ligand pairs; k_f is the forward binding rate, N_l is the ligand density on the particle surface; N_r is the receptors on the vessel wall; k_r is bond reverse binding rate.

The parameters used in our model are chosen according to physiological values reported in literature and are summarized in Table 1.

According to these parameters, the binding force for a single ligand-receptor bond is around 5 pN which is within the range of Bell's estimation (Bell 1978). In our simulation, NPs with adhesive force induced by the total bonds larger than drag force are assumed to be bonded to the wall.

3 Simulation results

3.1 Particle model

Different size and shape result in varying contact area of NPs and drag force induced by fluid, thus influencing NP binding process. Two representative shapes of NPs have been considered to investigate the geometric effect on particle deposition: spherical and rod-shaped particles. NPs with spherical and rod shape are illustrated in Fig. 1. Spherical particle is characterized by its diameter, whereas rod-shaped particles are characterized by the rod dimensions (w and L) and aspect ratio (γ). Nanorods of two different aspect ratios of 3 (γ = 3) and 5 (γ = 5) are considered. Volume of the nanorods is kept the same as the nanospheres to ensure the same drug load capacity. Dimensions of NPs used in the model are listed in Table 2.

3.2 Blood vessel model

Blood vascular network consists of many generations of vessels with decreasing diameter from parents to daughters. Besides diameter, the angle between two daughters at the branch varies, which leads to quite unique hydrodynamic conditions at each vessel tree. The angle of the bifurcation depends on the relative diameter of the daughter vessels (Wischgoll et al. 2009). In our model, the fluid domain contains one parent vessel and two daughter vessels, similar to those in previous publications (Barber et al. 2008; Xiong and Zhang 2012). Both the parent and daughter vessels are modeled as cylinders with constant diameters: 2 μm for parent vessel and 1 μm for daughter vessel. These small diameters are chosen because of the nanometer scale of the nanoparticles, which makes modeling in bigger channels computationally very expensive. The characteristics of the NP distribution are mainly influenced by local shear rates, rather than channel diameter. Branched angle (defined as the angle between the centerline of the parent vessel and the center line of the daughter) is chosen to be 45°. Due to cylindrical symmetry, only the longitudinal cross section is created to study the NP binding on its edge walls, as shown in Fig. 2. A rectangular region between 1 and 5 μm in x axis and a circular region with a diameter of 2 μm are chosen as the representative of the straight region and branched region, respectively, as shown in the Fig. 2b. The walls are set as non-slip boundaries, the inlet is applied with a parabolic fluid velocity profile and the outlets are open.

3.3 Shape dependent binding dynamics

Under a shear flow, spheres and rods exhibit different binding behaviors. The particle shape influences both initiation of adhesion and sustained binding after adhesion. Typical trajectories for a nanosphere and a nanorod are shown in Fig. 3.

First, initial contacts between NP and wall surface depend on particle shape. For spheres, their contact area is orientation irrelevant, with a constant binding area within interacting distance; for rods, while they might have higher chance of initiating contact due to larger length and tumbling motion, rod binding is orientation dependent with varying contact area. Under a low shear rate, it is expected that both spheres and rods bind immediately as they contact the wall by virtue of strong adhesion force since a single bond is larger than the drag force under low shear rate. At medium shear rate, the adhesion of a nanorod with point contact (when the nanorod is standing) with the wall is not enough to hold the particle and might be washed away easier as compared to a nanosphere. At a high shear rate, the bonding force of spheres cannot resist the drag force and will be washed away. In contrast, rods have a larger contact area with a reduced drag force when the principle long axis is aligned with the wall, thus has higher resistance and larger adhesion probability at high shear rate.

Second, the NP shape also influences the probability of NP to stay adhered or be washed away after initial adhesion. Decuzzi et al. (2006) studied the adhesive strength of non-spherical particles under shear flow. Assuming the particle is fixed along the surface, the attaching probability can be expressed as,

$$\frac{P_a}{m_r m_l K_a^0} = A_c \exp\left[-\frac{\lambda}{k_B T}\frac{F_{dis}}{m_r A_c}\right] \quad (10)$$

where K_a^0 is the association constant at zero load of the ligand-receptor pair; F_{dis} is the dislodging force due to hydrodynamic forces; m_r, and m_l are the receptor and ligand density, respectively; A_c is contact area; λ is the characteristic length of the ligand-receptor bonds; k_B is the Boltzmann constant; and T is the temperature. From Eq. (10), the normalized binding probability is plotted in Fig. 4 with a hypothesis of 100 % binding at shear rate of

zero at the centroid of NPs. As shown in Fig. 4, the rod with a higher aspect ratio ($\gamma = 5$) has the largest binding probability, whereas the sphere has the least binding probability. The difference becomes larger as NP size increases from 100 to 200 nm. It should be noted that the binding probability is based on the assumption that the long axis of nanorod is aligned with the binding surface, thus describes an equilibrium state rather than transitional state.

3.4 Distribution of nanoparticles of different shape and size under various shear rates

The shear rate at the vascular wall usually ranges from 250 to 2,000 s^{-1} at capillaries (Freitas 1999). To study the NP distribution under different flow conditions, simulations are performed for shear rates at the wall of 100, 200, 400, 600, and 1,000 s^{-1}, respectively, in the straight section. Accordingly, the shear rates at the bifurcation will be doubled based on the geometry.

At the inlet of the vessel, 200 nanospheres and nanorods are released at the core region (defined as 80 % of the vessel width at the center) of the vessel, respectively. The distribution of NPs on the vessel wall is recorded after flowing through the vessel once. No periodic boundary conditions are applied here. Two snapshots of the NP distribution are shown in Fig. 5. The binding density of 100 nm NPs over the whole channel is shown in Fig. 6, which exhibits many interesting phenomena.

First, a significant increase of particle density happens at about 6 μm from the inlet, which corresponds to where the mother vessel branches into daughter vessels and bifurcation begins. For example, rod shaped NPs ($\gamma = 3$) has a binding density of 30 bonds/μm at straight section but 65 bonds/μm at branched region at 400 s^{-1} in the bifurcation region. Such high binding density at branched region has been observed in all simulated cases except for the sphere at the highest flow rate of 500 μm/s, which corresponds to 1,000 s^{-1} shear rate at straight channel and 2,000 s^{-1} shear rate at branched region, as shown in Fig. 6e. The flow is deviated at the bifurcation point, which leads to a higher opportunity for NP to initiate contact with the channel wall. Figure 6e implies that the bonding force for spheres cannot resist the drag force from the blood at such high shear rate. The shear rate at the bifurcation is as high as 2,000 s^{-1}, which corresponds to an adhesion probability of around 15 %, as shown in Fig. 4a.

Second, NP binding rate decreases as shear rate increases. This is indicated by the decrease of the total number of bonded particles along the fluid channel from Fig. 6a–e. Higher shear rate increases the drag force exerted on the NP, thus leading to low binding. This observation is consistent with theoretical prediction shown in Fig. 4 and other experimental observations (Kona et al. 2012; Haun and Hammer 2008).

Third, the rod with aspect ratio 5 exhibits higher binding density at low shear rates (Fig. 6a–c), and lower binding density at higher shear rates (Fig. 6d–e). This is quite counterintuitive and different from the theoretical prediction shown in Fig. 4. Such behavior can be attributed to the competition between drag force and bonding force. At low shear rate, the binding force from a few ligand-receptor bonds is large enough to hold the particle. Nanorod has higher chance of contact with the wall, thus leading to higher binding probability. However, at high shear rate, the drag force and adhesion force exerted on the NPs depend on the orientation of the NPs. For example, if a rod has a point contact with the wall, it is subjected to a larger drag and smaller adhesion force, and is washed away easily. If NP is in contact with its long axis aligned with the wall surface, it may stay bonded with the wall due to relatively large adhesion force compared to drag force. This is evident from results shown in Fig. 7 through the snap shots of a sphere and a rod during the dynamic binding process.

Another interesting observation is the dynamic shifting in distribution of NPs at different shear rates. As the flow rate increases, the particle binding distribution tends to shift toward downstream, as indicated by the dashed dark lines marking the peak of distribution. More particles are bonded in the downstream, e.g., the particle density at 8 μm changes from 0 at shear rate of 200 s^{-1} to 20 bonds/ μm at 1,200 s^{-1}. At high shear rates, NP cannot bind firmly upon contact with the wall. Due to the tethering effect of receptor-ligand bonds, NP keeps rolling and tumbling along the surface until the adhesion force outweighs the drag force. Although some NPs will bind in the end, the final binding sites are different from their initial contact sites.

NPs of 200 nm are also simulated to study how NP size changes its distribution. The distributions of 200 nm NPs over different shear rates are shown in Fig. 8. Compared to 100 nm case shown in Fig. 6, the total number of bonded NPs decreases with increased particle size. At low shear rate, the NPs distribution is more non-uniform for 200 nm NPs compared to 100 nm NPs, with more NPs deposited at the bifurcation region. As the shear rate increases, the detachment of particles begins to happen at the bifurcation region. For example, detachment of spheres begins to happen at 1,200 s^{-1} at the bifurcation, which is lower than the 100 nm case. This is because larger NPs experience larger drag force at the same shear rate, thus they are easier to be detached. At shear rate of 1,200 s^{-1} in the bifurcation region, most spheres are unable to bind. At the highest shear rate of 2,000 s^{-1}, only rods with high aspect ratio of 5 are able to bind onto the wall. The binding density for both nanorod and nanosphere decreases over increased shear rate.

While adhesion plays an important role in NP binding after contact, the initialization of NP contact with wall is mainly determined by convection and diffusion. The fraction of NPs deposited on the straight section and the branched region is influenced by flow rate, NP diffusion speed and channel size, which could be characterized by the Péclet number (*Pe*) defined as:

$$Pe=\frac{LU}{D} \quad (11)$$

where L is the characteristic length of the channel, U is the corresponding fluid velocity, and D is the NP diffusion coefficient. In our model, L is chosen as 0.1 μm, D is calculated from Stokes–Einstein equation as 4.4×10^{-12} m^2/s and 2.2×10^{-12} m^2/s for 100 and 200 nm NPs, respectively.

To characterize the NP distribution, the ratio κ of the number of deposited NPs in branched region to straight section is plotted as a function of Péclet number, as shown in Fig. 9. When Péclet number is<1, diffusion is dominant so that most NPs bind at the straight section. As the Péclet number increases, convection becomes dominant, leading to higher binding density at the branched region. However, the ratio reaches the peak first and then decreases as Péclet number increases. This is because higher Péclet number means convection dominates, which makes NP difficult to marginate and bind to the wall. Shape also influences the distribution ratio. Spheres reach the peak ratio at the smallest Péclet number, followed by rod-shaped NPs with aspect ratio $\gamma = 3$, whereas NPs with aspect ratio $\gamma = 5$ have the peak ratio latest. This clearly shows that rods with high aspect ratio ($\gamma = 5$) are more resilient to high shear rate, whereas spheres have the worst adhesion at high shear rate.

4 Discussion and future work

The effect of nanoparticle size, shape, and vascular geometry on nanoparticle distribution is presented in the paper. The simulation results demonstrate that smaller NPs bind faster than bigger ones. This is because diffusion coefficient is proportional to the inverse of particle

size, thus diffusion speed for 100 nm particles is $\sqrt{2}$ times faster than 200 nm particles. Meanwhile, larger particles are subjected to large magnitude of drag force from fluid flow, which leads to lower binding probability. This conclusion is consistent with the statement that the critical shear stress required to remove adhered particles decreases as particles size increases (Cozens-Roberts et al. 1990b). The binding dynamics of rod-shaped NPs is initial contact and orientation dependent. Rod shaped NPs with larger aspect ratio do not necessarily have higher binding rate. This observation is quite different from the prediction of theoretical model (Decuzzi and Ferrari 2006). One assumption made in the theoretical model is that the long axis of non-spherical particles is aligned with the contact wall, which ensures the largest adhesion force with maximal contact area. In vivo, such idealized binding configuration does not always occur. The counter intuitive finding is consistent with other group's simulation, which states that the interaction between NPs and cells is particle initial contact orientation and local curvature dependent at the contact site (Yang and Ma 2010). Moreover, NP bond formation depends on the balance between adhesion and drag force. The drag force increases linearly with shear rate and results in lower binding probability of NPs at higher shear rate. The diverging flow at vessel bifurcations enables particles to have larger binding propensity, showing significantly enhanced binding at the bifurcation region. This finding is consistent with other published results for microparticles and leukocytes (Doshi et al. 2010; Tousi et al. 2010). Further, the percentage of NPs binding to the straight section and bifurcation region is found to be a function of Péclet number. When Péclet number is <1, diffusion is dominant, thus more particles are deposited at the straight section. As Péclet number increases, convection dominates over diffusion so that more particles are transported and deposited to the bifurcation region. For even larger Péclet number, the shear stress at the wall surpasses the critical shear stress for stable NP binding, leading to detachment of NPs.

One possible concern in the simulation is the choice of 2 μm vessel diameter, which is different from normal capillary with size between 5 and 10 μm. This choice is based on practical consideration for computational expense. In the immersed finite element method, for accurately capturing the fluid velocity around the NP, the fluid element size should be less than the solid element size. To reach a certain NP concentration [order of 10^8/mL (Haun and Hammer 2008)], more particles should also be put into the fluid region in a bigger vessel. This leads to a high demand on computation and memory storage. The total number of mesh elements needed could be as high as tens of millions, which drastically decreases computational speed. In order to analyze if the NP binding results are sensitive to vessel size, a larger vessel 10 μm wide and 50 μm long is created. In the simulation, nanospheres with the same concentration (8.6×10^8/mL) used in 2 μm vessel are released at the core region of the vessel. The shear rate at the bifurcation is kept at 200 s^{-1}, the same as that used in the 2 μm vessel case. Since the vessel size is increased to 10 μm, the average flow velocity is increased to 250 μm/s in order to keep the same shear rate at the wall. NP binding distribution for the 10 μm vessel shows that the distribution characteristics are the same as smaller size vessels, i.e., higher binding density at bifurcation region and specific locations of peak binding density, as shown Fig. 10. While the key characteristics are consistent, there are a few slight differences in binding density for vessels of different sizes. The larger vessel diameter increases the diffusion time for NPs to marginate toward the wall, leading to a lower binding density on the wall after flowing once. The higher flow velocity for larger vessel transports more particles to the bifurcation and slightly increases the binding density at bifurcation. The more supply of NPs in the larger vessel also increases the NP binding density at the daughter vessels, as shown in the binding density after 40 μm in Fig. 10a. Yet, the key factor that influences NP binding is the local shear rate, rather than vessel size (Decuzzi and Ferrari 2006; Chang et al. 2000). Thus, the conclusion that preferential binding occurs at the bifurcation is generally applicable vessels of microvasculature. Indeed, the preferential binding at the bifurcation is also reported by other

research groups in vessels range between 25 and 100 μm (Doshi et al. 2010; Tousi et al. 2010).

In our model, the particle distribution is studied at microscale where motion of individual particle is tracked and the binding dynamics is described with details of ligand-receptor bonds. However, to predict large scale overall in vivo distribution, a higher scale continuum model is required to characterize NP convection, diffusion and reaction. In the continuum model, particle binding will be described in terms of NP concentration, diffusion coefficient, shear rate, reaction rates, etc. How to link the microscale particulate model with the continuum model will be an interesting topic to explore in the future. A multiscale model consisting of continuum model of organ level and particulate model of cellular level will be beneficial to NP distribution prediction and drug dosage administration.

In conclusion, the simulation results show that NP binding is particle size, shear rate and vessel geometry dependent. The binding rate is higher for NPs of smaller sizes, at lower shear rates and at vessel bifurcations. The ratio of bound NPs between straight region and bifurcation region depends on the Péclet number. The simulation results will contribute to the rational design of drug nanocarriers that have different sizes and shapes and that targeted to the tissue with many bifurcation vessels.

Acknowledgments

The authors acknowledge the supports of this work from NSF CAREER Grant CBET-1113040 and NIH grant EB009786.

References

Almeida JPM, Chen AL, Foster A, Drezek R. In vivo biodistribution of nanoparticles. Nanomedicine. 2011; 6(5):815–835. [PubMed: 21793674]

Barber J, Alberding J, Restrepo J, Secomb T. Simulated two-dimensional red blood cell motion, deformation, and partitioning in microvessel bifurcations. Ann Biomed Eng. 2008; 36(10):1690–1698. [PubMed: 18686035]

Bell G. Models for the specific adhesion of cells to cells. Science. 1978; 200(4342):618–627. [PubMed: 347575]

Bell GI, Dembo M, Bongrand P. Cell adhesion. Competition between nonspecific repulsion and specific bonding. Biophys J. 1984; 45(6):1051–1064. [PubMed: 6743742]

Chang K-C, Tees DFJ, Hammer DA. The state diagram for cell adhesion under flow: leukocyte rolling and firm adhesion. Proc Nat Acad Sci. 2000; 97(21):11262–11267. [PubMed: 11005837]

Chauvierre C, Labarre D, Couvreur P, Vauthier C. Novel polysaccharide-decorated poly(isobutyl cyanoacrylate) nanoparticles. Pharm Res. 2003; 20(11):1786–1793. [PubMed: 14661923]

Chen H, Ruckenstein E. Nanoparticle aggregation in the presence of a block copolymer. J Chem Phys. 2009; 131(24):244904–244907. [PubMed: 20059112]

Chen H, Ruckenstein E. Aggregation of nanoparticles in a block copolymer bilayer. J Colloid Interface Sci. 2011; 363(2):573–578. [PubMed: 21875712]

Cho K, Wang X, Nie S, Chen Z, Shin DM. Therapeutic nanoparticles for drug delivery in cancer. Clin Cancer Res. 2008; 14(5):1310–1316. [PubMed: 18316549]

Christian DA, Cai S, Garbuzenko OB, Harada T, Zajac AL, Minko T, Discher DE. Flexible filaments for in vivo imaging and delivery: persistent circulation of filomicelles opens the dosage window for sustained tumor shrinkage. Mol Pharm. 2009; 6(5):1343–1352. [PubMed: 19249859]

Cozens-Roberts C, Lauffenburger DA, Quinn JA. Receptor-mediated cell attachment and detachment kinetics. I. Probabilistic model and analysis. Biophys J. 1990a; 58(4):841–856. [PubMed: 2174271]

Cozens-Roberts C, Quinn JA, Lauffenberger DA. Receptor-mediated adhesion phenomena. Model studies with the radical-flow detachment assay. Biophys J. 1990b; 58(1):107–125. [PubMed: 2166596]

Decuzzi P, Ferrari M. The adhesive strength of non-spherical particles mediated by specific interactions. Biomaterials. 2006; 27(30):5307–5314. [PubMed: 16797691]

Decuzzi P, Godin B, Tanaka T, Lee SY, Chiappini C, Liu X, Ferrari M. Size and shape effects in the biodistribution of intravascularly injected particles. J Control Release. 2010; 141(3):320–327. [PubMed: 19874859]

Doshi N, Prabhakarpandian B, Rea-Ramsey A, Pant K, Sundaram S, Mitragotri S. Flow and adhesion of drug carriers in blood vessels depend on their shape: a study using model synthetic microvascular networks. J Control Release. 2010; 146(2):196–200. [PubMed: 20385181]

Einstein, A. Investigations on the theory of Brownian Movement. Fürth, R., editor; Cowper, AD., translator. Dover Publ; New York: 1956. (1926, reprinted 1956)

Ermak DL, Mccammon JA. Brownian dynamics with hydrodynamic interactions. J Chem Phys. 1978; 69(4):1352–1360.

Farokhzad OC, Langer R. Nanomedicine: developing smarter therapeutic and diagnostic modalities. Adv Drug Deliv Rev. 2006; 58(14):1456–1459. [PubMed: 17070960]

Freitas, RA., Jr, editor. Nanomedicine. Volume I: basic capabilities. Landes Bioscience; Georgetown: 1999.

Geng Y, Dalhaimer P, Cai S, Tsai R, Tewari M, Minko T, Discher DE. Shape effects of filaments versus spherical particles in flow and drug delivery. Nat Nanotechnol. 2007; 2(4):249–255. [PubMed: 18654271]

Gentile F, Ferrari M, Decuzzi P. The transport of nanoparticles in blood vessels: the effect of vessel permeability and blood rheology. Ann Biomed Eng. 2008; 36(2):254–261. [PubMed: 18172768]

Haun JB, Hammer DA. Quantifying nanoparticle adhesion mediated by specific molecular interactions. Langmuir. 2008; 24(16):8821–8832. [PubMed: 18630976]

Hoganson DM, Howard PI II, Spool ID, Burns OH, Gilmore JR, Vacanti JP. Principles of biomimetic vascular network design applied to a tissue-engineered liver scaffold. Tissue Eng Part A. 2010; 16(5):1469–1477. [PubMed: 20001254]

Kona S, Dong J-F, Liu Y, Tan J, Nguyen KT. Biodegradable nanoparticles mimicking platelet binding as a targeted and controlled drug delivery system. Int J Pharm. 2012; 423(2):516–524. [PubMed: 22172292]

Lee TR, Chang YS, Choi JB, Liu WK, Kim YJ. Numerical simulation of a nanoparticle focusing lens in a microfluidic channel by using immersed finite element method. J Nanosci Nanotechnol. 2009; 9(12):7407–7411. [PubMed: 19908798]

Li A, Ahmadi G. Dispersion and deposition of spherical-particles from point sources in a turbulent channel flow. Aerosol Sci Tech. 1992; 16(4):209–226.

Li M, Panagi Z, Avgoustakis K, Reineke J. Physiologically based pharmacokinetic modeling of PLGA nanoparticles with varied mPEG content. Int J Nanomed. 2012; 7:1345–1356.

Liu Y, Liu WK, Belytschko T, Patankar N, To AC, Kopacz A, Chung JH. Immersed electrokinetic finite element method. Int J Numer Meth Eng. 2007; 71(4):379–405.

Liu J, Weller GER, Zern B, Ayyaswamy PS, Eckmann DM, Muzykantov VR, Radhakrishnan R. Computational model for nanocarrier binding to endothelium validated using in vivo, in vitro, and atomic force microscopy experiments. Proc Nat Acad Sci. 2010; 107(38):16530–16535. [PubMed: 20823256]

Liu Y, Tan J, Thomas A, Ou-Yang D, Muzykantov VR. The shape of things to come: importance of design in nanotechnology for drug delivery. Ther Deliv. 2012; 3(2):181–194. [PubMed: 22834196]

Longest PW, Kleinstreuer C. Comparison of blood particle deposition models for non-parallel flow domains. J Biomech. 2003; 36(3):421–430. [PubMed: 12594990]

Mathiowitz E, Jacob JS, Jong YS, Carino GP, Chickering DE, Chaturvedi P, Santos CA, Vijayaraghavan K, Montgomery S, Bassett M, Morrell C. Biologically erodable microsphere as potential oral drug delivery system. Nature. 1997; 386(6623):410–414. [PubMed: 9121559]

Mitragotri S, Lahann J. Physical approaches to biomaterial design. Nat Mater. 2009; 8(1):15–23. [PubMed: 19096389]

Mody NA, King MR. Influence of Brownian motion on blood platelet flow behavior and adhesive dynamics near a planar wall. Langmuir. 2007; 23(11):6321–6328. [PubMed: 17417890]

Mori N, Kumagae M, Nakamura K. Brownian dynamics simulation for suspensions of oblong-particles under shear flow. Rheol Acta. 1998; 37(2):151–157.

Muro S, Garnacho C, Champion JA, Leferovich J, Gajewski C, Schuchman EH, Mitragotri S, Muzykantov VR. Control of endothelial targeting and intracellular delivery of therapeutic enzymes by modulating the size and shape of ICAM-1-targeted carriers. Mol Ther. 2008; 16(8):1450–1458. [PubMed: 18560419]

Muzykantov VR, Radhakrishnan R, Eckmann DM. Dynamic factors controlling targeting nanocarriers to vascular endothelium. Curr Drug Metab. 2012; 13(1):70–81. [PubMed: 22292809]

Nasongkla N, Bey E, Ren JM, Ai H, Khemtong C, Guthi JS, Chin SF, Sherry AD, Boothman DA, Gao JM. Multifunctional polymeric micelles as cancer-targeted, MRI-ultrasensitive drug delivery systems. Nano Lett. 2006; 6(11):2427–2430. [PubMed: 17090068]

Peppas NA. Intelligent biomaterials as pharmaceutical carriers in microfabricated and nanoscale devices. MRS Bull. 2006; 31(11):888–893.

Prabhakarpandian B, Pant K, Scott R, Patillo C, Irimia D, Kiani M, Sundaram S. Synthetic microvascular networks for quantitative analysis of particle adhesion. Biomed Microdevices. 2008; 10(4):585–595. [PubMed: 18327641]

Roney C, Kulkarni P, Arora V, Antich P, Bonte F, Wu AM, Mallikarjuana NN, Manohar S, Liang HF, Kulkarni AR, Sung HW, Sairam M, Aminabhavi TM. Targeted nanoparticles for drug delivery through the blood–brain barrier for Alzheimer's disease. J Control Release. 2005; 108(2–3):193–214. [PubMed: 16246446]

Saad Y, Schultz MH. Gmres—a generalized minimal residual algorithm for solving nonsymmetric linear-systems. Siam J Sci Stat Comp. 1986; 7(3):856–869.

Sanhai WR, Sakamoto JH, Canady R, Ferrari M. Seven challenges for nanomedicine. Nat Nano. 2008; 3(5):242–244.

Shah P. Use of nanotechnologies for drug delivery. MRS Bull. 2006; 31(11):894–899.

Shah S, Liu Y. Modeling particle shape-dependent dynamics in nanomedicine. J Nanosci Nanotechnol. 2011; 11(2):919–928. [PubMed: 21399713]

Sharma N, Patankar NA. Direct numerical simulation of the Brownian motion of particles by using fluctuating hydrodynamic equations. J Comput Phys. 2004; 201(2):466–486.

Shuvaev VV, Ilies MA, Simone E, Zaitsev S, Kim Y, Cai S, Mahmud A, Dziubla T, Muro S, Discher DE, Muzykantov VR. Endothelial targeting of antibody-decorated polymeric filomicelles. ACS Nano. 2011; 5(9):6991–6999. [PubMed: 21838300]

Stolnik S, Illum L, Davis SS. Long circulating microparticulate drug carriers. Adv Drug Deliv Rev. 1995; 16(2–3):195–214.

Sukhorukov GB, Mohwald H. Multifunctional cargo systems for biotechnology. Trend Biotechnol. 2007; 25(3):93–98.

Tan J, Thomas A, Liu Y. Influence of red blood cells on nanoparticle targeted delivery in microcirculation. Soft Matter. 2012; 8(6):1934–1946. [PubMed: 22375153]

Tousi N, Wang B, Pant K, Kiani MF, Prabhakarpandian B. Preferential adhesion of leukocytes near bifurcations is endothelium independent. Microvasc Res. 2010; 80(3):384–388. [PubMed: 20624406]

Ward MD, Hammer DA. A theoretical analysis for the effect of focal contact formation on cell-substrate attachment strength. Biophys J. 1993; 64(3):936–959. [PubMed: 8386020]

Wischgoll T, Choy JS, Kassab GS. Extraction of morphometry and branching angles of porcine coronary arterial tree from CT images. Am J Physiol Heart Circu Physiol. 2009; 297(5):H1949–H1955.

Xiong W, Zhang J. Two-dimensional lattice Boltzmann study of red blood cell motion through microvascular bifurcation: cell deformability and suspending viscosity effects. Biomech Model Mechanobiol. 2012; 11(3):575–583. [PubMed: 21744014]

Yang K, Ma Y-Q. Computer simulation of the translocation of nanoparticles with different shapes across a lipid bilayer. Nat Nano. 2010; 5(8):579–583.

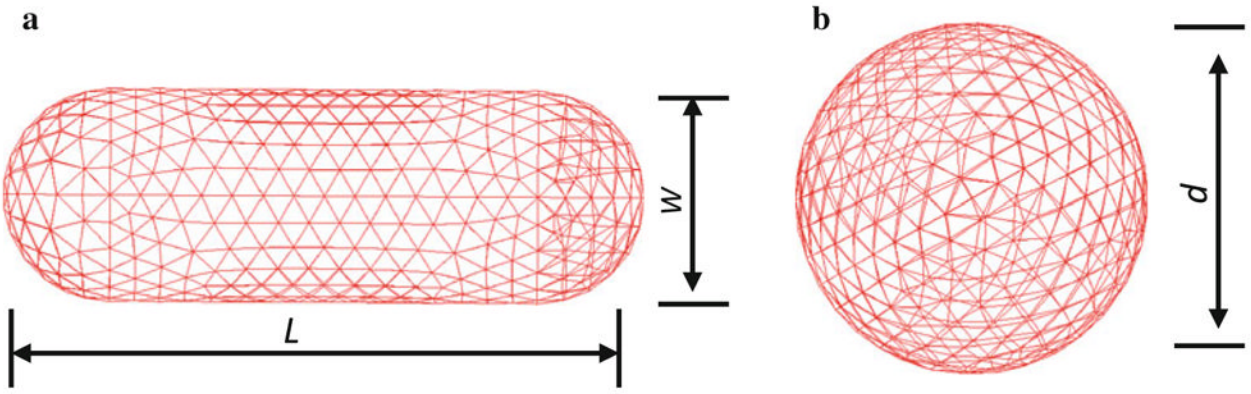

Fig. 1.
Illustrations of rod and sphere particles: **a** rod, **b** sphere, respectively

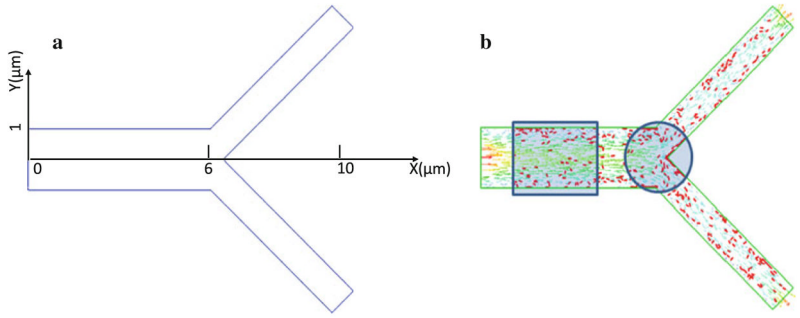

Fig. 2.

A bifurcation microchannel for NP deposition simulation. **a** Dimensions of the geometry, **b** the region defined as straight section and bifurcation area

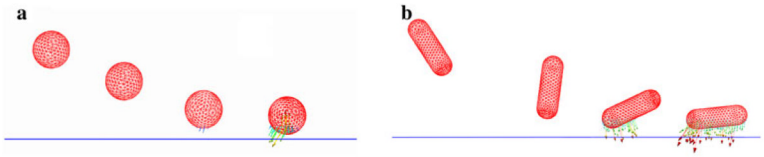

Fig. 3.
Trajectory snapshots of a nanosphere (**a**) and a nanorod (**b**) under shear flow. The *arrows* illustrate the adhesive force once the particles interact with the wall

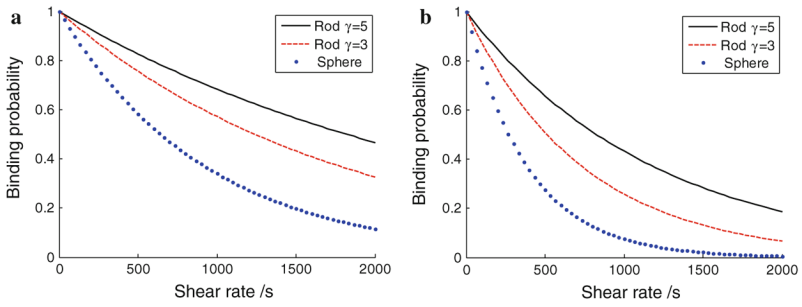

Fig. 4.
Normalized binding probability for **a** NP size of 100 nm; **b** NP size of 200 nm

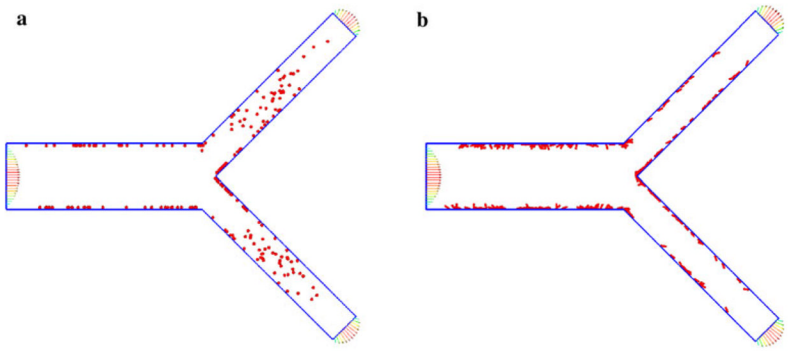

Fig. 5.
A snap shot of the particle distribution in the branched vessel for **a** spheres; **b** rods

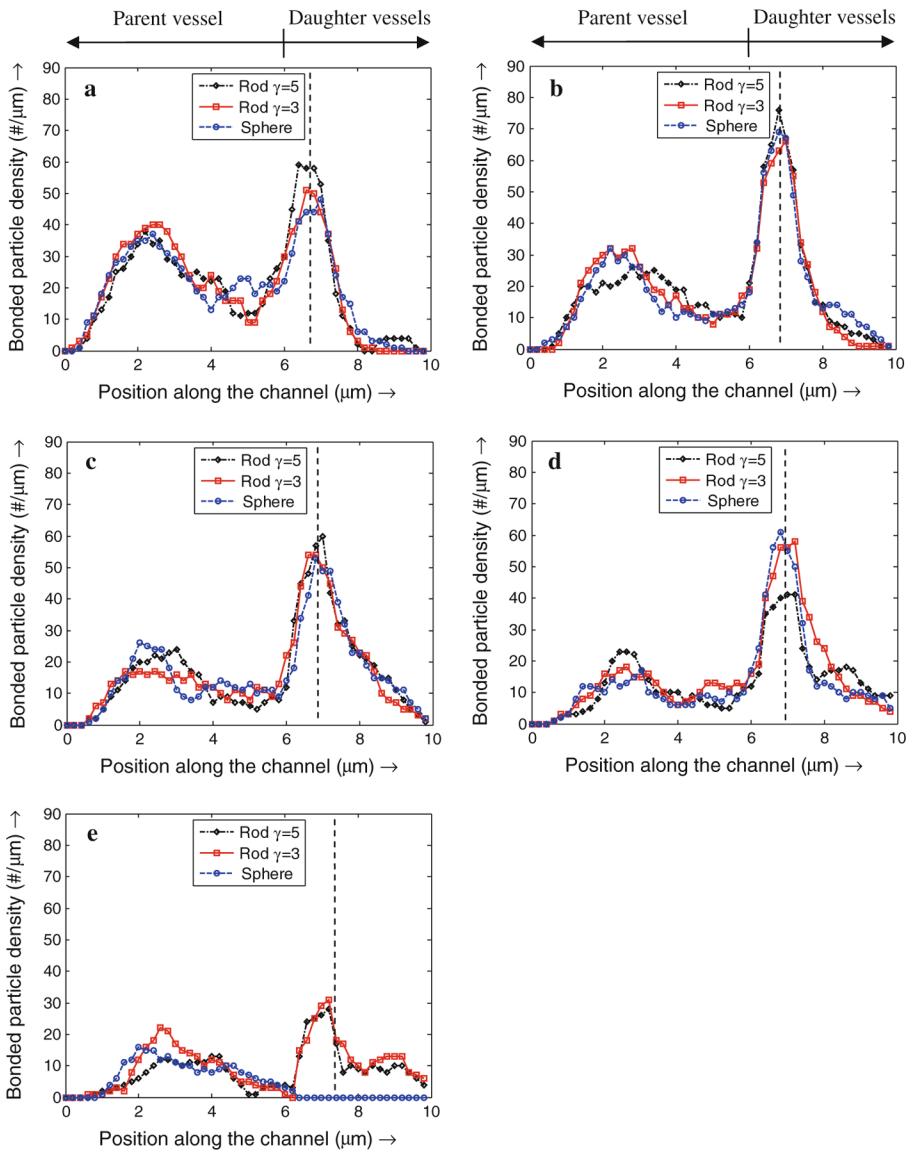

Fig. 6.

100 nm nanoparticle distribution along the channel. Shear rates at the bifurcation region are **a** 200 s^{-1}, **b** 400 s^{-1}, **c** 800 s^{-1}, **d** 1,200 s^{-1}, **e** 2,000 s^{-1}

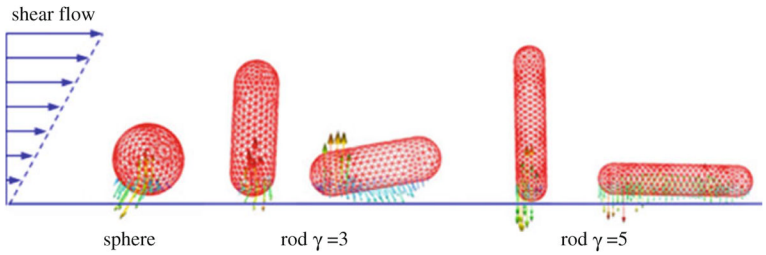

Fig. 7.

Adhesion of NPs depends on particle shape and their orientation. Nanorods have smaller contact area and bonding force during transient rotation, but with maximal bonding force after laying down with long axis aligned with wall

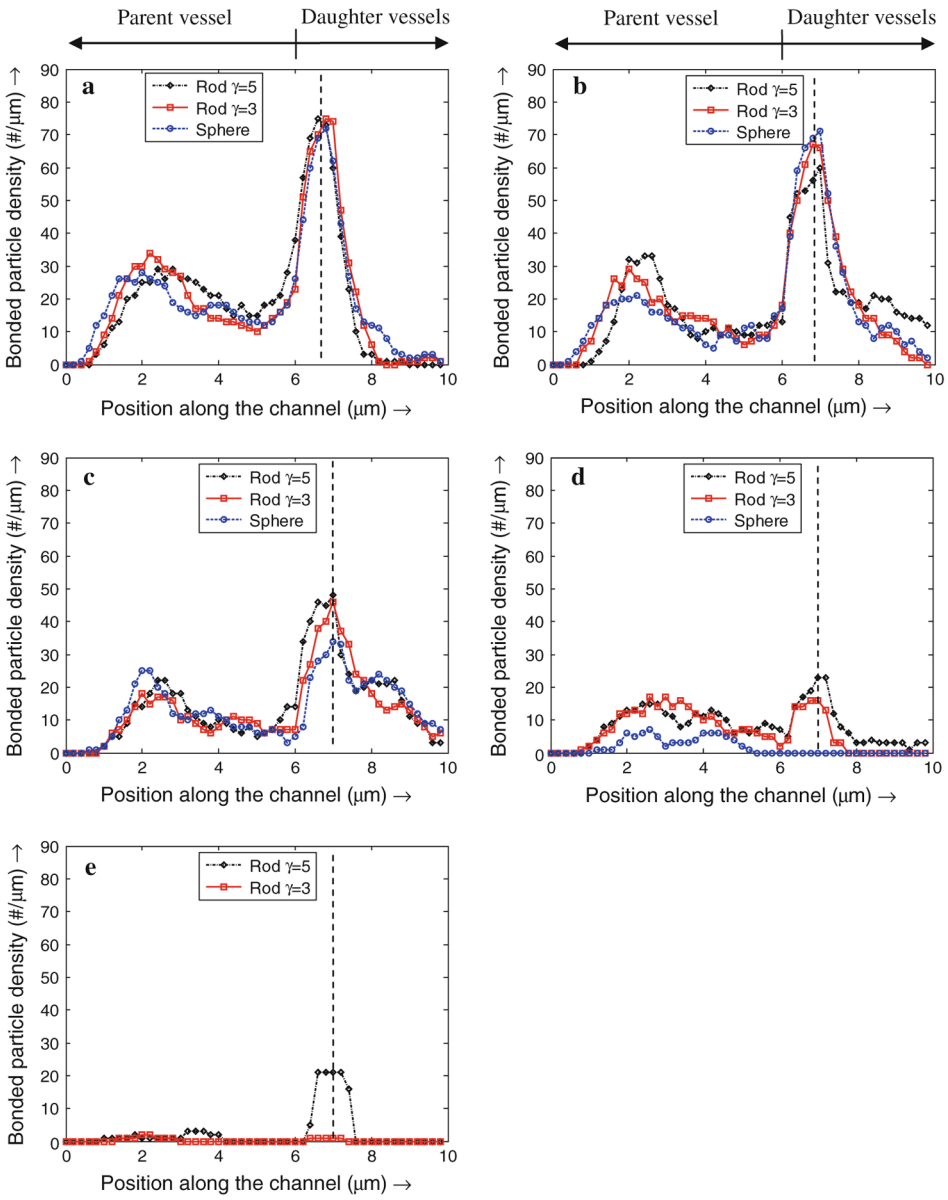

Fig. 8.

200 nm nanoparticle distribution along the channel. Shear rates at the bifurcation region are **a** 200 s^{-1}, **b** 400 s^{-1}, **c** 800 s^{-1}, **d** 1,200 s^{-1}, **e** 2,000 s^{-1}

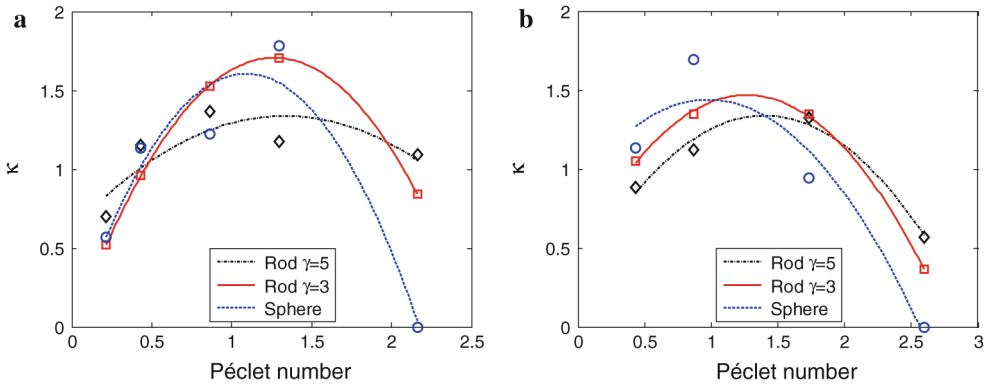

Fig. 9.

Ratio of the number of deposited NPs on branched region and straight section depends on the Péclet number. The simulation data are fitted by quadratic lines through least square method. **a** 100 nm NPs; **b** 200 nm NPs

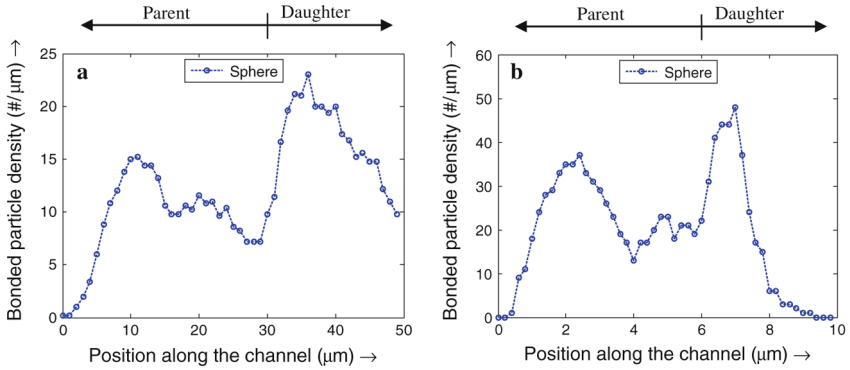

Fig. 10.

100 nm NP distribution along a channel with width of 10 μm (**a**) and 2 μm (**b**) with a shear rate of 200 s^{-1} at the bifurcation

Table 1

Parameters used in the receptor ligand binding model

Parameters	Value	References
Ligand density N_l	200/μm^2	Ward and Hammer (1993)
Receptor density N_r	100/μm^2	Ward and Hammer (1993)
Unstressed bond length L	20 nm	Bell (1978), Bell et al. (1984)
Bond spring constant	0.5 dyn/cm	Ward and Hammer (1993)
Forward binding rate k_f	1×10^6 nm^2/s	Cozens-Roberts et al. (1990a)
Reverse binding rate k_r	$1 \times 10^{-2}/s$	Cozens-Roberts et al. (1990a)

Table 2

Dimensions of nanorods and nanospheres

Sphere	**Rod (γ = 3)**		**Rod (γ = 5)**	
d (nm)	w (nm)	L (nm)	w (nm)	L (nm)
100	63	189	52	261
200	126	378	104	522